Advanced Functional Materials

ADVANCED FUNCTIONAL MATERIALS
www.afm-journal.de

RESEARCH ARTICLE OPEN ACCESS

Amyloidogenic Peptide Fragments Designed From Bacterial Collagen-like Proteins Form Hydrogel

Vamika Sagar[1,2] | Xuen J Ng[1] | Lukas Lechel[1] | Ashish Chand Rajwar[1] | Hendrik Bargel[1] | Abhishek A. Jalan[1]

[1]Department of Biomaterials, University of Bayreuth, Bayreuth, Germany | [2]Integrated Structural Biology Department, Institut de Génétique et de Biologie Moléculaire et Cellulaire, Illkirch, France

Correspondence: Abhishek A. Jalan (jalan@cantab.net)

Received: 8 December 2025 | **Revised:** 8 January 2026 | **Accepted:** 19 January 2026

Keywords: amyloids | bacterial collagen-like proteins | biocompatible | biomaterials | peptide hydrogels

ABSTRACT

Bacterial collagen-like proteins (CLPs) are composed of tandem Gly-*X*-*Y* sequence repeats, but, unlike metazoan collagens, their *X*- and *Y*-positions are enriched in hydrophobic and polar residues rather than proline. This distinctive sequence bias suggests that CLPs may harbor sequence features that could promote amyloid-like assembly. Using bioinformatic screening of CLPs, we identified amyloidogenic motifs enriched in alanine, isoleucine, leucine, or valine at the *X*-position and threonine at the *Y*-position. Guided by these findings, we designed a focused library of peptides incorporating Gly-*X*-Thr triplet and the highly abundant GATGVT sextet repeats. Peptides containing Gly-*X*-Thr produced insoluble fibers, restricting exploration of material properties. In contrast, peptides containing GATGVT repeats formed micrometer-long fibers that physically crosslinked into a robust hydrogel upon centrifugation. Circular dichroism (CD) and Fourier Transform Infrared Spectroscopy (FTIR) revealed length-dependent variations in secondary structure. Imaging of the higher-order structures confirmed densely packed fiber networks while rheological measurements indicated sequence-length-dependent viscoelastic behavior. Notably, a 30 residue GATGVT peptide hydrogel supported high in vitro cell viability of fibroblasts. Overall, these findings suggest that CLPs are an underexplored reservoir of sequence motifs with promising biomaterial potential.

1 | Introduction

The bacterial proteome is an inexhaustible source of biomaterials due to the sheer diversity of bacterial species and the unique proteins they express for survival in different environments [1]. The structural diversity and tunability of such proteins make the proteome a vast and diverse library of biological building blocks for biomaterials [2]. Of particular interest are proteins that form higher-order amyloid-like structures that can be reprogrammed to develop new structural materials such as adhesives [3, 4], and biocompatible scaffolds [5, 6]. Such proteins, called functional amyloids, often rely on imperfect tandem sequence repeats to stabilize fibers and control aggregation [7].

For example, the Curli protein CsgA found in enteric bacteria such as *Escherichia coli* contains five imperfect repeats of ~19–23 amino acid long sequences that drive amyloid formation via stacking of β-strands [8]. Similarly, the core amyloid protein FapC from *Pseudomonas* species contains three asparagine/glutamine-rich tandem repeats that drive amyloidogenesis. Further, TasA from *Bacillus subtilis* contains two tandem amyloidogenic stretches within the N-terminal half crucial for amyloid-like fibrils [9]. Other prominent examples include Bap [10] and Esp [11] proteins, which also contain imperfect tandem repeats that drive amyloidogenesis. The imperfect tandem repeats in these proteins constitute the core of the amyloids and thus are able to form amyloid fibrils in vitro when expressed

recombinantly or as peptides. For example, LNIYQY, VTQVGF, and IYGYGG hexapeptides derived from the R1, R2, and R3 repeats of CsgA, respectively, form steric zipper fibrils [12]. This reductionist approach, where short fragments of proteins known to be amyloidogenic in the native state can also form amyloids in vitro, is crucial to our ability to develop new biomaterials. Thus, identifying more such proteins or fragments that can form amyloid-like fibers can provide fine-tuned control over self-assembly characteristics, mechanics, and functionality. Similarly, the tandem repeats in biofilm-associated proteins (Bap) found in several *Staphylococcus*, *Salmonella*, and *Pseudomonas* species share a common STVTVTF motif with some variability in the first and last sequence position. This specific heptameric peptide, contained within the C-repeats of the Bap from *Staphylococcus epidermidis*, forms amyloid fibrils with β-sheet secondary structure [13]. Similarly, the N-terminus GNNQQNY and its truncated analogue NNQQNY from yeast prion protein Sup35p self-assemble into amyloid fibrils with cross-β structure [14]. Other examples of short peptides within the context of tandem sequences that form amyloids are known [7].

Metazoan collagens share a characteristic structural motif called a triple helix, which contains three supercoiled polypeptides [15]. The polypeptides are composed of tandem repeats of Gly-*X*-*Y* with glycine in every third position, *X* frequently proline, and *Y* its post-translationally modified analogue 4-hydroxyproline [16]. Based on similarity to the Gly-*X*-*Y* triplet repeat, many proteins in other taxonomic groups, such as bacteria [17] and viruses [18] have been annotated as collagen-like proteins (CLPs) [18]. We have recently shown that the frequency of amino acids in the *X*- and *Y*-positions varies between the taxonomic groups [19]. In particular, the sequence of bacterial CLPs diverges significantly from that in eukaryotic collagens [17]. Proline no longer dominates the *X*-position, which is now predominantly occupied by alanine, while the *Y*-position is overwhelmingly threonine. Such tandem repeats of alternating hydrophobic and polar amino acids are a characteristic feature of amyloid-forming regions across many proteins. In the case of bacteria, threonine residues in some bacterial CLPs have been shown to be glycosylated [20–24]. While this post-translational modification (PTM) is crucial for their ability to form triple helices [25] and contribute to biofilm formation [26] and sporulation [22, 24], it likely also prevents the native sequences from forming β-sheets.

Several examples of full-length proteins that do not form amyloid-fibrils but contain fragments that are amyloidogenic have been reported [27]. Such aggregation-prone regions are either sequestered into the protein core [28], shielding them from pairing with other regions to initiate aggregation, or are post-translationally modified [29, 30] to sterically prevent nucleation of aggregation. Such aggregation hotspots can be frequently identified using bioinformatic tools [31, 32]. Motivated by these observations, we hypothesized that peptides containing tandem repeats composed of Gly-*X*-Thr repeats might form β-sheet rich amyloid-like fibrils that transition to interesting higher-order structures. To this end, we bioinformatically investigated all known bacterial CLPs and identified sequence features that could enable amyloid-like fibrillation and higher-order assembly. We then designed peptides that incorporate these sequence features and, using a combination of secondary structure and morphology analysis, establish that they form fibers and ultimately bio-compatible hydrogels. Our results indicate that bacterial CLPs sequences are an underexplored but potentially rich source of features that may offer promising opportunities for biomaterial development and applications.

2 | Results

2.1 | Amyloidogenic Propensities of Fragments from Collagen-like Proteins

In order to identify sequence features from bacterial CLPs that could be exploited to design amyloidogenic peptides, we isolated the collagen-like domains from bacterial CLPs and assessed their amyloidogenic potential using four prediction tools—Aggregation Nucleation Prediction in Peptides and Proteins (ANuPP) [33], CANYA [34], Prediction of Amyloid Structural Aggregation 2.0 (PASTA2) [35] and TANGO [36]. ANuPP is an ensemble machine-learning classifier trained on experimentally validated amyloid-forming hexapeptides. CANYA employs a convolution-attention hybrid neural network trained on a very large experimentally validated dataset of 100 000 aggregating peptides. On the other hand, PASTA2.0 calculates pairwise interaction energy for self-interacting pairs of potential β-strands along the sequence based on statistical potentials obtained from a large experimental dataset. TANGO employs a statistical mechanical algorithm to compute aggregation propensity based on physicochemical properties such as hydrophobicity, hydrogen-bonding, and charge patterns. Thus, the four methods differ in how they predict the amyloidogenic potential of a sequence. With the exception of ANuPP, which gives a binary output of whether or not a sequence contains amyloidogenic fragments, all the remaining tools output scores. We obtained scores from CANYA, PASTA2.0, and TANGO for collagen-like domains of CLPs, extracted the top 1% scoring sequences, and assessed the relative abundance of amino acids in the *X*- and *Y*-positions. In the case of ANuPP, we collected all sequences predicted to contain amyloidogenic fragments. As shown in Figure 1, threonine dominates the Y-position in all highly scoring fragments, and the *X*-position experiences variable abundances of predominantly hydrophobic amino acids alanine, valine, isoleucine, and leucine in that order.

Based on this observation, we hypothesized that peptides containing Gly-*X*-T repeats, where *X* is alanine, isoleucine, leucine, or valine, might exhibit aggregation tendencies and form β-sheet-rich fibrillar assemblies reminiscent of amyloid structures. To test this, we designed a small, focused library of peptides containing either GAT, GLT, GVT, or GIT triplets. Close inspection of CLPs that score in the top 1% with the amyloid prediction tools revealed several examples of GAT triplet followed or preceded by GVT. Further analysis suggests that G[A/V]G[A/V]T is the most abundant among all sextet repeats (Figure S1). To test the amyloidogenic potential of GATGVT, we obtained peptides containing the sextet with length equal to those in the (Gly-*X*-Thr)$_n$ series (Table 1). To systematically understand how sequence length affects secondary structure propensity and higher-order self-assembly, shorter peptides containing 2-6 GATGVT repeats were obtained. The length of all peptides was capped to 14 repeats or 42 amino acids due to the ease of peptide synthesis using solid phase approach.

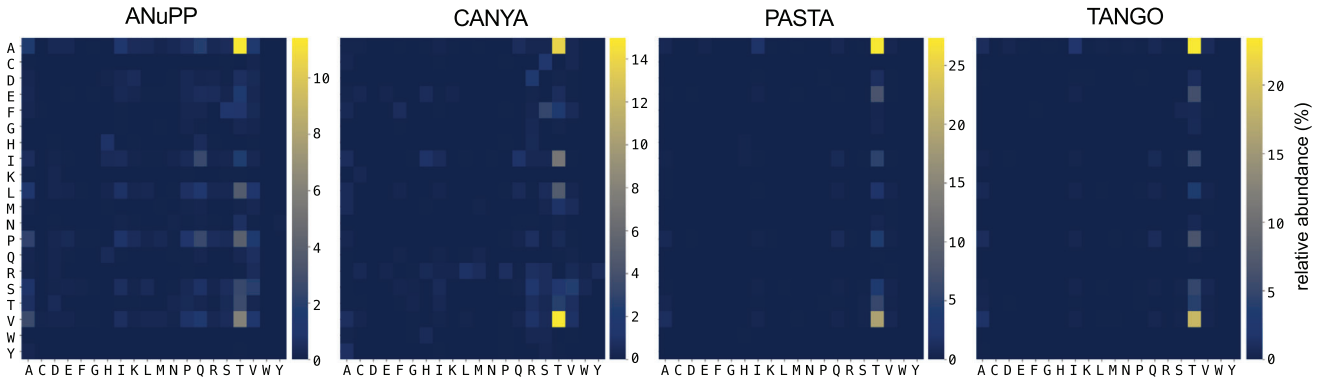

FIGURE 1 | Amyloidogenic propensities of collagen-like domains in bacterial CLPs. Heatmaps showing the relative abundance of amino acids in the *X*- and *Y*-positions of Gly-*X*-*Y* repeats extracted from bacterial CLPs that are predicted to be amyloidogenic by four independent tools—ANuPP, CANYA, PASTA2.0, and TANGO. For ANuPP, all sequences identified as containing amyloidogenic were included, while for the remaining tools, only the top 1% scoring sequences were analyzed. The *x*- and *y*-axes represent the relative frequency of amino acids in the *X*- and *Y*-positions, respectively.

TABLE 1 | Peptides sequences employed in this study and their acronyms.

Acronym	Peptide sequence
(Gly-*X*-Thr)$_n$	
GAT-42	Ac-(GAT)$_{14}$-NH$_2$
GLT-42	Ac-(GLT)$_{14}$-NH$_2$
GIT-42	Ac-(GIT)$_{14}$-NH$_2$
GVT-42	Ac-(GVT)$_{14}$-NH$_2$
GVT-30	Ac-(GVT)$_{10}$-NH$_2$
GVT-18	Ac-(GVT)$_6$-NH$_2$
(Gly-*X*-Thr-Gly-*Y*-Thr)$_n$	
GATGVT-42	Ac-(GATGVT)$_7$-NH$_2$
GATGVT-36	Ac-(GATGVT)$_6$-NH$_2$
GATGVT-30	Ac-(GATGVT)$_5$-NH$_2$
GATGVT-24	Ac-(GATGVT)$_4$-NH$_2$
GATGVT-18	Ac-(GATGVT)$_3$-NH$_2$
GATGVT-12	Ac-(GATGVT)$_2$-NH$_2$

2.2 | Physical State and Secondary Structures Suspensions of (Gly-X-T)$_n$ Peptides

Peptide GAT-42 was soluble in aqueous buffer, and its CD analysis did not reveal any secondary structure features except random coil within the employed concentration range (Figure 2). It is known that glycosylation of threonine induces a peptide containing 10 repeats of GPT to form a triple helix, while the unmodified sequence remains a random coil [25]. The glycosylation of the G-*X*-T sequence is also established in bacterial collagen-like glycoproteins found in the exosporium of some organisms of the *Bacillus cereus* family [24, 37]. It is likely that this PTM facilitates folding into the quaternary structure, though the exact mechanism remains unclear. The GAT peptide is fully soluble and adopts a random coil conformation as indicated by CD. Since these results suggested an inability to form fibers or hydrogels under our experimental conditions, and were unlikely to present any promising features from a biomaterials perspective, we did not investigate it further.

The crude peptides of GIT-42, GVT-42, and GLT-42 had limited solubility in water that improved only marginally upon ultrasonication for >30 min. The suspensions obtained after ultrasonication had a viscous consistency, i.e., the suspension did not flow readily when we inverted the Eppendorf tubes. We centrifuged the suspensions to separate the supernatant and obtained a dense phase that had gel-like consistency for both GIT-42 and GVT-42. The CD spectra of these gels resuspended in Milli-Q water revealed β-sheet signature (Figure 2), and the AFM revealed micrometer-long fibers (Figure S2). To understand if we could improve solubility and guide gelation at the same time by changing the pH and temperature, we dialyzed the GIT-42 and GVT-42 suspensions of crude peptides against phosphate (pH 6.9), tris-HCl (pH 7.2), and citrate buffer (pH 3.8) at 5°C. Dialysis did not significantly change the physical state of GIT-42, and it was unable to form gel under these conditions. However, GVT-42 formed a hydrogel in citrate buffer. The gel disintegrated upon manual handling with a spatula suggesting a low yield strength. In the hope of increasing the structural integrity of this hydrogel, we lowered the sequence length of the GVT peptide from 42 to 30 and 18 amino acids. Both GVT-30 and GVT-18 remained only partially soluble, and dialysis against citrate buffer at pH 3.8 again resulted in a weak hydrogel similar to GVT-42. The CD spectra of both shorter peptides indicated random coil conformation, while the featureless AFM images of GVT-18 were consistent with this observation. However, the AFM image of GVT-30 shows fibers that were micrometer in length (Figure S2). Since these analyses were conducted with crude samples, it is impossible to conclude if the fibers result from the peptides or unknown impurities. We attempted to purify the GVT peptides by dissolving their crude forms in 6 M guanidinium thiocyanate. GdmSCN is a strong chaotrope that denatured the aggregates rendering all three peptides fully soluble. However, all peptides formed copious aggregates upon dialysis against Milli-Q water.

The GLT-42 peptide also had limited solubility in Milli-Q water, but it did not result in a gel upon centrifugation. We diluted

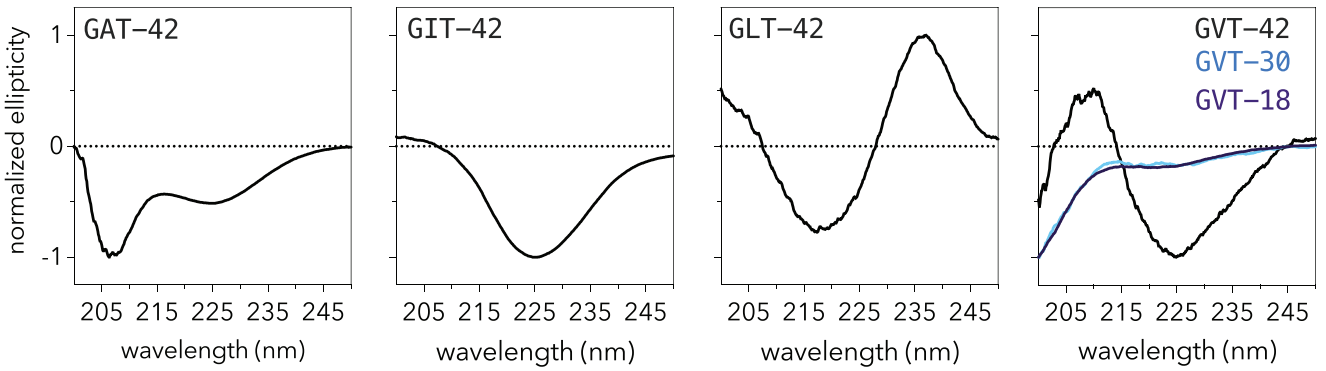

FIGURE 2 | Secondary structures of (Gly-X-Thr)$_n$ peptides. CD spectrographs of the GAT-42, GIT-42, and GLT-42 peptide gels resuspended in Milli-Q water, and that of GVT-42, GVT-30, and GVT-18 peptides after dialysis in citrate buffer at pH 3.8, resulting in a weak hydrogel. In order to facilitate visual comparison of the spectral shape, the ellipticity of each spectrum is normalized with the absolute maximum intensity set to unity.

TABLE 2 | Solubility and habitus of the (GATGVT)$_n$ peptide solutions pre- and post-dialysis.

Peptides	Solubility—Pre-dialysis	Solubility—Post-dialysis
GATGVT-12	Large aggregates	Large aggregates
GATGVT-18	Clear solution	Clear solution
GATGVT-24	Moderately soluble—slurry	Viscosity increases
GATGVT-30	Moderately soluble—slurry	Viscosity increases
GATGVT-36	Moderately soluble—slurry	Viscosity increases
GATGVT-42	Clear solution	Translucent, slightly viscous

the suspension obtained in the dense phase in Milli-Q water. This revealed an intriguing CD spectrum with a maximum at ~240 nm and a minimum at ~ 220 nm. The spectral shape as well as the position of the maximum and minimum are reminiscent of the CD spectrum of streptavidin, which contains antiparallel β-sheets that fold into a β-barrel [38]. It is likely that the GLT-42 spectrum is convoluted by the assembly of β-sheet secondary structures into a higher-order tertiary or quaternary structure. Such convolutions resulting in variations in spectral shape have been frequently observed in β-sheet rich proteins [39]. The AFM of GLT-42 was largely featureless, which rendered it less interesting from a biomaterial perspective (Figure S2). Despite our best efforts, we could not obtain purified peptides for testing gelation. We conclude that the inability of our Gly-*X*-Thr peptides to form robust hydrogels is likely due to their intrinsic biochemical properties that do not support formation of entangled fiber networks and not due to suboptimal experimental conditions.

2.3 | Physical State and Secondary Structures in (Gly-X-Thr-Gly-Y-Thr)$_n$ Peptides

The solubility of the GATGVT peptides depended on the sequence length in a non-linear fashion. The 42 and 18 aa sequences were fully soluble in water, 24–36 aa sequences were partly soluble, while the 12 aa sequence was largely insoluble. We were able to purify the 18-42 aa crude peptides via dialysis. The physical state of the peptides as observed in the dialysis tubes after 2 days depended on the sequence length (Table 2 and Figure 3).

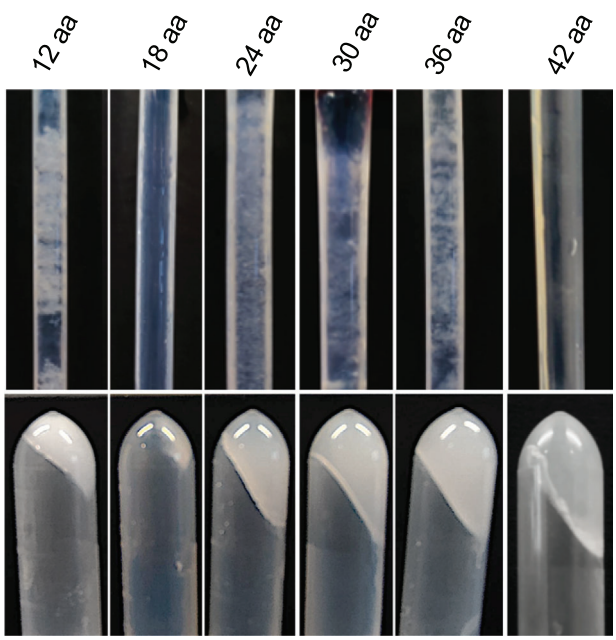

FIGURE 3 | Physical state of the (GATGVT)$_n$ suspensions. The images show length-dependent changes in aggregation propensity during dialysis (top) and gels obtained after centrifugation (bottom) for the (GATGVT)$_n$ peptides.

GATGVT-18 formed a clear solution, GATGVT-12 formed copious aggregates, GATGVT of 24-36 sequence length formed a moderately soluble viscous slurry, and GATGVT-42 had a viscous

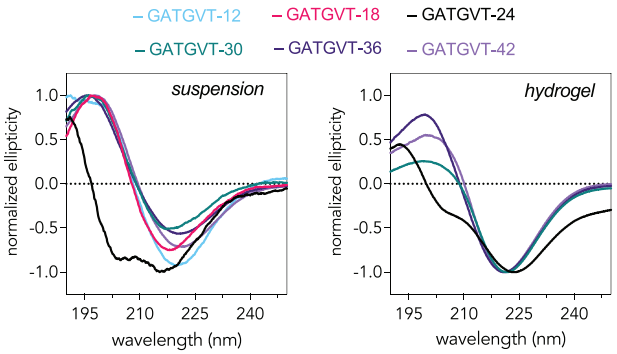

FIGURE 4 | Secondary structure of $(GATGVT)_n$ peptides. Secondary structure changes in peptides of the GATGVT series in the dialyzed suspension (left) and after centrifugation (right). The ellipticity of each spectrum is normalized with the absolute maximum intensity set to unity for comparison.

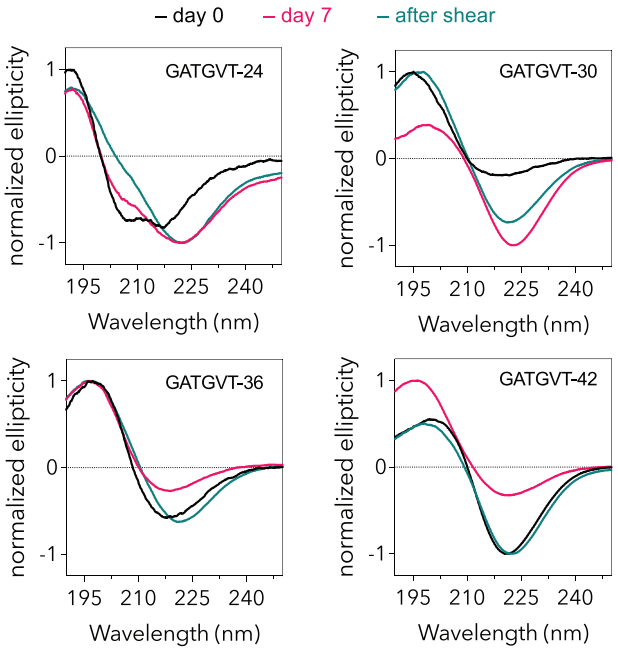

FIGURE 5 | Time- and shear-dependent changes in secondary structure within hydrogels. CD spectra of hydrogels obtained on the day of centrifugation, after storing the gels at 5°C for 7 days, and after applying shear stress on a rheometer.

and moderately translucent appearance. Previously, peptide and protein suspensions have been compacted into hydrogels using centrifugation, which presumably crosslinks the higher-order structures to create a physically entangled network that traps water. For example, silk fibroin nanofibrils and amyloidogenic peptides have been physically crosslinked into a hydrogel using centrifugation [40]. Upon centrifugation, GATGVT-12 resulted in a compacted dense phase without gel-like consistency, while GATGVT-18, which was the most soluble among all peptides, did not result in a gel. The other four peptides formed hydrogels upon centrifugation and could be manually handled without significantly compromising their integrity. Presumably, our peptide suspensions have some degree of network connectivity. Upon applying a centrifugal field, the suspended particulates are packed at the bottom of the tube, increasing local volume fraction until the network propagates and behaves as a physical gel supported by both physical entanglement and non-covalent interactions. Following this promising lead, we analyzed the secondary structure characteristics of the gels using a combination of CD and FTIR and fibril morphology using AFM and SEM.

2.4 | Secondary Structures in the GATGVT Suspensions and Hydrogels

The hydrogels obtained from centrifugation were scraped with a pipette tip, resuspended in ~200 μL of Milli-Q water via vortexing, and the suspensions were analyzed using CD and FTIR. As shown in Figure 4, the CD spectra of all suspensions and hydrogels except GATGVT-24 are consistent with β-sheets. The CD spectrum of GATGVT-24 suspension shows two prominent minima at ~205 and 215 nm with $[\theta]_{215}$ / $[\theta]_{205}| > 1$. The positions of the minima, as well as their intensity ratio, are indicative of α-helices. However, both minima are blue-shifted in comparison to the typically observed values of 208 and 222 nm. These shifts could result from a combination of factors, including conformational change due to compaction, where helices are packed into higher-order structures, or scattering from these structures. The relative ratio of the minima increases significantly with a concomitant red-shift towards the β-sheet minimum in the hydrogel (Figure 4). Thus, the α-helical signature may also represent kinetically trapped metastable states that ultimately revert to the thermodynamic minimum represented by the β-sheets.

To further understand the source of this shift, we incubated all hydrogels for a week and obtained CD spectra. For most peptides, incubation changes the ratio of the minima and maxima with a moderate red shift in the maxima while the spectral signatures remain consistent with β-sheets (Figure 5). However, GATGVT-24 shows an increase in $[\theta]_{215}$ / $[\theta]_{205}|$ ratio and the minima at 215 nm red shift toward β-sheet values. Peptides can get kinetically trapped into α-helical conformation that revert to the thermodynamically more stable β-sheets [41, 42]. This transformation can be affected by time or by providing mechanical energy in the form of shear during centrifugation. To explore this, we subjected the hydrogel samples incubated for a week to shear on a rheometer. The CD spectra before and after applying shear stress in a rheometer are similar in shape profile for all peptides except GATGVT-24 (Figure 5). GATGVT-24 shows a further lowering of the $[\theta]_{215}/[\theta]_{205}|$ ratio while the 215 minimum is now firmly in the region expected for β-sheets. While these are not incontrovertible proof of a conformational change, it does suggest that the initial α-helical secondary structure is under kinetic control and that time or shear results in a change to the thermodynamically more stable β-sheets.

FTIR is a sensitive method for discriminating between the secondary structures. It can also distinguish between parallel and anti-parallel β-sheets, β-turns/loops, and strongly hydrogen-bonded β-sheet as in the case of extended β-aggregates with reasonable certainty. The spectrograph corresponding to the amide I band (1700–1600 cm^{-1}) provides detailed information on the secondary structures of the peptides. Especially, the second derivative plot of the amide I band reveals hidden peaks that allow

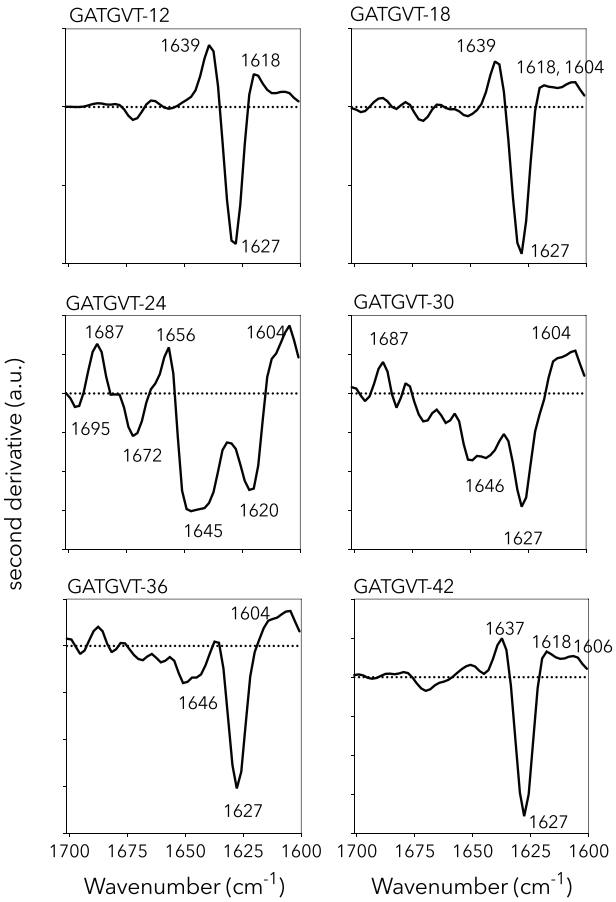

FIGURE 6 | Secondary structure analysis using FTIR. Second derivative curves of the ATR-FTIR spectra of all 6 peptides in the GATGVT series obtained in Milli-Q water. The maxima and minima in the peaks were manually determined based on the peak intensity. (A.U. = arbitrary units).

a more fine-tuned interpretation of the secondary structures [43]. We obtained FTIR spectra of the dense phase obtained after centrifugation i.e., both the aggregates and gels in Milli-Q water (Figure 6).

The aggregate of the shortest peptide GATGVT-12 and the hydrogel of the longest peptide GATGVT-42 show similar spectral profiles with a dominant maximum at 1627, indicating β-sheets, and weak maxima at 1618 and 1604–1606 cm^{-1}, often associated with β-sheet aggregates. The spectrum of GATGVT-18 is also consistent with β-sheets, but additional higher frequency bands between 1700 and 1675 cm^{-1} point to antiparallel β-sheet components. The spectral profiles of GATGVT-30 and GATGVT-36 are similar across the entire frequency range, with minima at 1627 cm^{-1} for β-sheets and a higher frequency band at ~1646 cm^{-1} associated primarily with disordered regions and turns, with possible α-helical contributions. This suggests a moderate degree of secondary-structure heterogeneity hydrogels of both peptides, a feature not apparent in the CD spectra, which predominantly show β-sheet signatures. In contrast, the bands in the GATGVT-24 spectra are consistent with a mixture of antiparallel β-sheet and helical/turn, indicating large-scale conformational heterogeneity that is also observed in the CD spectra. Overall, these data indicate that all peptides ultimately adopt β-sheet-rich assemblies, but that the balance between ordered β-sheets and disorder/turn-like structures is strongly dependent on peptide length. This length-dependent structural plasticity is likely to be an important determinant of the self-assembly pathways and material properties of the resulting hydrogels, as we discuss below.

2.5 | Higher-Order Structures Supporting the Hydrogel

The higher-order structures present within hydrogels of the GATGVT peptides were analyzed using AFM and SEM. As shown in Figure 7, all four peptides form micrometer-long flexible fibers of high aspect ratio. While a quantitative determination of the fibril dimensions was not feasible due to extensive bundling, qualitatively the GATGVT-24 and GATGVT-42 appear to form shorter fibers, GATGVT-36 shows a larger distribution of fiber length and GATGVT-30 forms relatively longer fibers. SEM images generally reveal a dense laterally packed phase with very little porosity. Whether the lack of porosity is due to the drying effect, where fibers pack laterally due to capillary forces, or due to syneresis when water is expelled due to centrifugal force is not immediately clear to us. The SEM micrograph of GATGVT-24 gel displays moderate porosity, while all the remaining peptides do not contain discernible pores. Thus, it appears that the decreased porosity is likely a result of syneresis. The high degree of lateral packing of the fibers indicates strong attractive non-covalent interactions between fibrils. When centrifugal force is applied, these attractive interactions allow the fibrillar network to collapse and efficiently expel water.

2.6 | Viscoelastic Properties of GATGVT Hydrogels

The viscoelastic properties of GATGVT-24 to -42 gels obtained by centrifugation at 13.3xG were investigated using a rheometer. Specifically, oscillating amplitude sweeps were measured, from which the storage (G') and loss (G") modulus as a function of applied strain at a constant frequency of 1 Hz were obtained. In all cases, the gels had a G' higher than G" in the low strain regime (< 0.1%), indicating a higher elastic contribution and solid characteristics at rest. Notably, all gels displayed a very short linear viscoelastic region, which was exceeded upon reaching strains over 0.2%. Both findings align with the petroleum-like characteristics of gels observed during handling (Figure 8).

Deducing the strain at maximum oscillation stress, we observed that all gels exhibited similar strains at maximum in the range of 15%–20% strain, with the highest average strain measured for GATGVT-24. However, the respective maximum stress measured was highest for GATGVT-24 (2260 Pa ± 1751 Pa), whereas average values for GATGVT-30 to -36 were in a similar regime (30-aa: 701 ± 516 Pa, 36-aa: 915 ± 831 Pa, and 42-aa: 815 ± 635 Pa, respectively). Interestingly, comparing the strain of the cross-over moduli, the strain at which the viscous contribution exceeded the elastic contribution and hence indicating the flow point of the hydrogels, GATGVT-24, -30 and -42 showed similar strains at the cross-over point with GATGVT-30 gels in average exhibiting the highest strain at the flow point (24-aa: 81.3 ± 29.9%, 30-aa: 93.45 ± 88.88% and 42-aa: 72.8 ± 66.2%) while GATGVT-36 gels were found with the lowest strain (36-aa: 39.1 ± 15.89%) at the flow point. This finding supports the previously stated observation

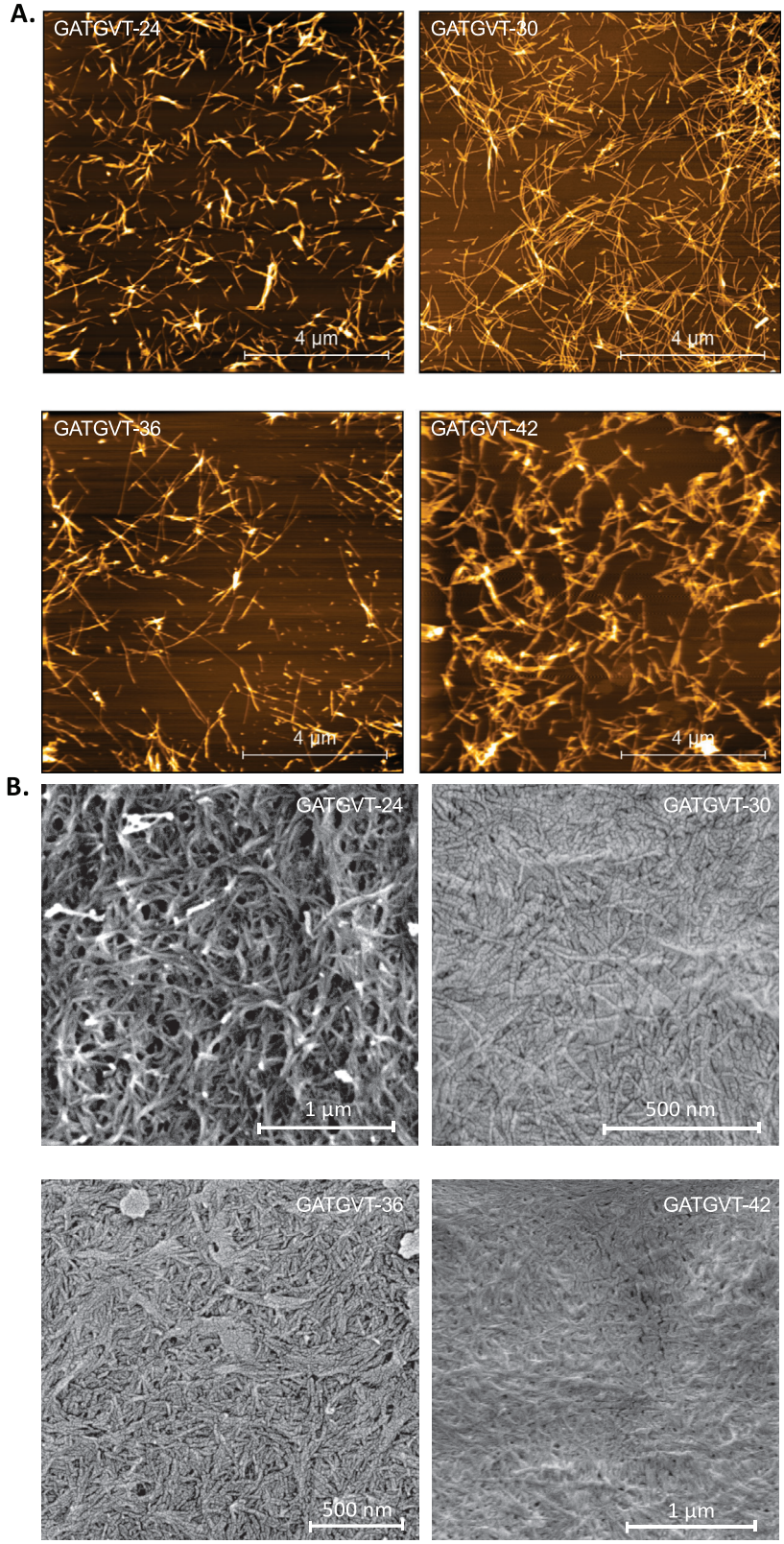

FIGURE 7 | Fibril morphology within hydrogels. AFM height image (A) and SEM micrographs (B) of hydrogel-forming peptides GATGVT-24, GATGVT-30, GATGVT-36, and GATGVT-42.

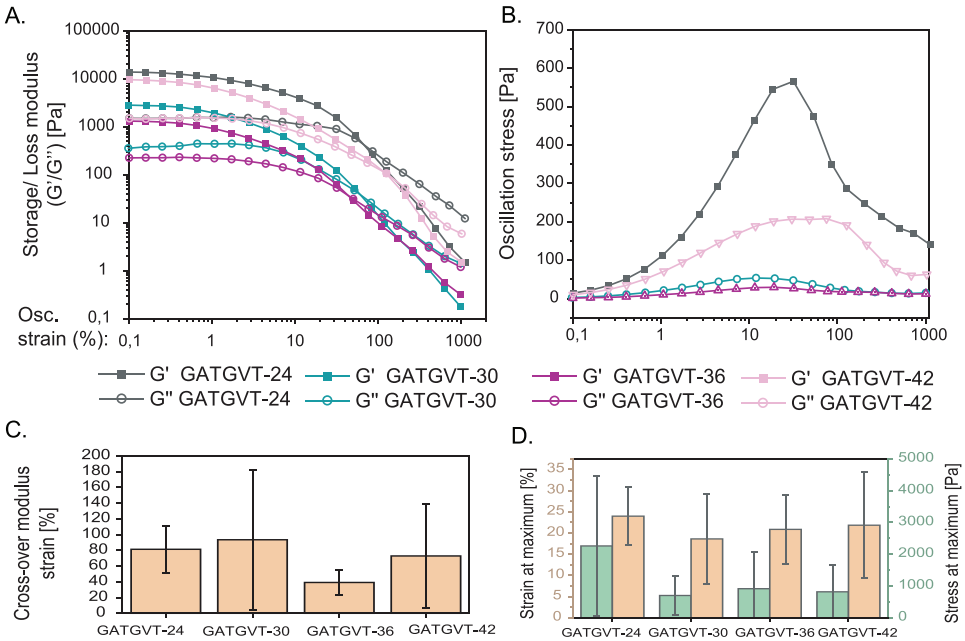

FIGURE 8 | Viscoelastic gel properties of GATGVT gels. Representative amplitude sweep curves showing storage and loss moduli (A) and stress (B) as a function of strain measured at 1 Hz. Strain at the cross-over point of the storage and loss moduli (C) and maximum stress and strain (D), which were deduced from amplitude sweep experiments.

that lowering the sequence length could contribute to hydrogel integrity and potentially reflects the apparent distribution of fiber morphologies observed by AFM. GATGVT-30 shows the most extended cross-over point due to the presence of longer fibers and hence stronger entanglement compared to GATGVT-36, which had a mixed distribution of fiber sizes, limiting packing density and bulk entanglement. Notably, this data can only be considered as an approximation of the aforementioned observations on fiber morphology identified by AFM, as non-linear material behavior in the large amplitude oscillation strain regime does not follow the same assumptions for the stress response as in the small amplitude oscillation strain regime [44] and an in-depth analysis was beyond the scope of this work.

2.7 | The GATGVT-30 Hydrogel is Biocompatible

To elucidate cytocompatibility of GATGVT gels, we chose a NIH/3T3 mouse fibroblast cell line for basic characterization [45–48] by seeding cells on the gels and conducting a live-dead assay, which is based on the turnover of calcein-AM by metabolically active cells (= alive, green) and intercalating of ethidium homodimer to accessible DNA (= dead, red). The GATGVT-30 peptide was chosen for the live-dead assay, as this peptide is a sweet spot considering the sequence length, fiber length, and the hydrogel structural integrity to provide an ambient environment for cell growth. The result of the live/dead staining clearly showed that the gel yields cell viability (Figure 9). The cell count increased exponentially through the week with a negligible increase in the number of dead cells. Over a week, cell multiplication resulted in clusters of live cells, which we suspect to be tissue-like structures. These clusters were not evenly distributed throughout the gel, likely a result of the difference in packing density of the gel. Therefore, the cell migration in the peptide hydrogels is uneven.

3 | Discussion

Proteins from several taxonomic groups contain sequences that are characterized by tandem repeats composed of alternating polar and nonpolar amino acids. Such protein domains have a high amyloidogenic tendency. Specifically, bacteria contain several such proteins that play a central role in biofilm formation [49–51]. These proteins are called functional amyloids [7], contrasting them against pathogenic amyloids implicated in many human conditions. At the sequence level, the proteins that form functional amyloids contain imperfect tandem repeats of low sequence complexity, frequently rich in patterns of polar and nonpolar amino acids. Presumably, the variations in the number of repeats modulate amyloid fibril structure and mechanical properties, imperfections in the sequence guard against excessive aggregation propensity, and the polar-nonpolar patterns promote anti-parallel beta-sheet secondary structure.

Many bacterial CLPs bear similarities to functional amyloid-forming proteins with respect to repetitiveness, sequence imperfections within the repeats, and abundance of polar-nonpolar amino acid patterns. In the context of native organisms, such CLP domains are subject to PTMs and are present as part of multidomain constructs, which likely prevents CLPs from forming amyloids. Inspired by this information, we here designed collagen-like peptides containing perfect tandem repeats of polar and nonpolar sequence complexity that have a strong tendency to form beta-sheet fibrils and ultimately hydrogels (Table 3).

In these peptides, the nature of hydrophobic amino acids as well as the number of tandem repeats distinguishes non-specific aggregation from well-formed beta-sheet fibrils. Branched-chains amino acids isoleucine, leucine, and valine in the *X*-position of Gly-*X*-T repeats predominantly result in low solubility fibrillar

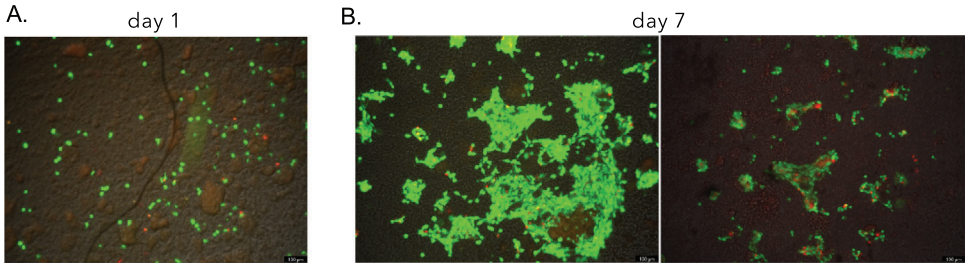

FIGURE 9 | Biocompatibility of hydrogels. Live/dead staining of the fibroblast cells on day 1 (A) and day 7 (B), showing the distribution of the live (green) and dead (red) cells on the GATGVT-30 hydrogel. The images are representative of two replicates performed with independently prepared gels.

TABLE 3 | Summary of the solubility, gelation tendency, secondary structures, and morphological features of the peptides presented in this study.

Peptide	Solubility	Gelation	CD	FTIR	AFM
GAT-42	Yes	No	Random coil	—	—
GLT-42	Insoluble	No	*β*-sheet	—	Aggregates
GIT-42	No	No	*β*-sheet	—	Fibres
GVT-42	Partially	Weak	*β*-sheet	—	Fibres
GVT-30	Partially	Weak	Random coil	—	Fibres
GVT-18	Partially	Weak	Random coil	—	Aggregates
GATGVT-42	Yes	Yes	*β*-sheet	Beta-sheet	Fibres
GATGVT-36	Partially	Yes	*β*-sheet	Beta-sheet, Disordered, Turns	Fibres
GATGVT-30	Partially	Yes	*β*-sheet	Beta-sheet, Disordered, Turns	Fibres
GATGVT-24	partially	Yes	α-helix, *β*-sheet	α-helix, *β*-sheet	Fibres
GATGVT-18	Yes	No	*β*-sheet	Likely antiparallel *β*-sheet	Aggregates
GATGVT-12	No	No	*β*-sheet	*β*-sheet	Fibres

aggregates, while alanine alone results in a fully soluble random coil peptide that does not undergo higher-order assembly. Peptides that contain alternating patterns of alanine and valine in the Gly-*X*-T repeat form fibers and hydrogels. The morphology of the fibers, their secondary structures, and the mechanical strength of the hydrogel are dependent on the number of triplet repeats. In general, shorter peptides tend to form fibers, but do not form hydrogels.

Many other examples of self-assembling peptides that contain perfect tandem repeats have been reported. For example, the RAD16 and EAK16 peptides containing two repeats of ARADADAR and EAEAKAKA repeats form *β*-sheet fibers and hydrogels driven by ionic interactions [52, 53]. Another prominent example is the elastin-like polypeptides containing tandem repeats of VPGVG that form a unique *β*-spiral with extended nanoporous structures [54]. The tandem repeat peptides also show a length-dependent variation in mechanical properties, consistent with our observations. For example, amphipathic oligopeptides containing repeats of FKEE form *β*-sheet fibrils, and their hydrogels show a length-dependent variation in sheer moduli and also the nature of charged and hydrophobic groups [55].

Compared to beta-sheet rich hydrogels formed by silk proteins, which undergo self-assembly and secondary structure changes mediated by hydrophobic interactions, the major difference is seemingly the macroscopic hydrogel structure and flow behavior. Silk proteins form rigid and brittle hydrogels [56], which is evident by a long linear viscoelastic region followed by a rapid drop of the storage modulus, once exceeding the yield point, shortly after followed by a cross-over of storage and loss modulus [57]. The gels obtained from the collagen-like peptides used in this study exhibited a short linear viscoelastic region but an extended region until the cross-over point was reached, underlining the differences in the structure and flow properties compared to other beta-sheet based hydrogels such as those obtained from silk and silk-inspired proteins. The gels formed start to flow rapidly, and fibrils align parallel to the direction of shear rather than undergoing fracturing and the formation of microcracks, which is usually evident by an increase in the loss modulus exceeding the yield point.

4 | Conclusion

The Gly-*X*-*Y* repeat sequence common to metazoan collagens and CLPs across diverse taxonomic groups [15, 58, 59] is known to form the characteristic triple-helical structural motif [60]. The stability of the triple helix is strongly dependent on a high abundance of proline residues [16], which likely also prevents exploration of other secondary structures. Inspired by the tandem repeats found in bacterial proteins known to form functional amyloids, we hypothesized that the tandem Gly-*X*-*Y* repeat sequence

devoid of proline and abundant in an alternating pattern of hydrophobic and polar amino acids in the *X*- and *Y*-position, respectively, could also form amyloids. Bioinformatic analysis of bacterial CLPs revealed amyloidogenic fragments with preferential abundance of alanine, isoleucine, leucine and valine in the *X*- and threonine in the *Y*-position. Peptides containing tandem repeats of Gly-*X*-T were observed to form amyloid-like fibrils and, in some cases, biocompatible hydrogels in a sequence-type and length-dependent fashion. We have explored only a small portion of the sequence space vis-à-vis residues in the *X*- and *Y*-positions that could form amyloids. It is likely that other combinations of hydrophobic amino acids, substituting threonine for serine and sextet repeats containing leucine and isoleucine could improve the structural properties of the fibers and hydrogels. While scouting amino acids for generating amyloid-forming peptides, we relied on a rudimentary method of selecting residues that are preferentially populated in bacterial CLPs and were scored highly by the amyloid prediction tools. An in-depth search of the top scoring sequences could further reveal additional fragments, with perhaps mixed abundance of residues in both sequence positions, that expand the material properties of the amyloid fibrils and hydrogels and find broad applicability as biomaterials.

5 | Methods and Experiments

5.1 | Identifying Amyloidogenic Sequences from Bacterial CLPs

We queried UniProtKB database on 16.12.2024 for sequences annotated by InterPro to contain collagen-like sequence repeats in bacteria. The query term was "(taxonomy_id:2) AND (xref:interpro-ipr008160)", which resulted in 8923 protein sequences. We clustered these sequences at 70% redundancy using CD-HIT [61] to exclude those with high sequence similarity, resulting in 8314 unique sequences. We then removed sequences that contained unknown sequence identifier such "X" or "B" and obtained 8215 sequences. From these sequences, we extracted collagen-like domains as those containing 6 or more contiguous repeats of Gly-*X*-*Y* repeats while disallowing three or more continuous occurrences of glycines within the domain. This resulted in 14022 collagen-like domains, which were saved as FASTA format file and uploaded to ANuPP (https://web.iitm.ac.in/bioinfo2/anupp/homeseq1/) and PASTA2.0 (http://old.protein.bio.unipd.it/pasta2/) webservers. The ANuPP webserver allows "prediction of amyloidogenic hexapeptides" and "identification of amyloidogenic-prone regions (APR) in protein sequences". We used the latter option with the default threshold of 0.52. ANuPP gives a binary output labelling amyloidogenic sequences as "True" or "False". We extracted all collagen-like domains identified as "True" to determine the relative abundance of residues in the *X*- and *Y*-positions. In the case of PASTA2.0 webserver, we used the "peptide" threshold with predefined top pairing energies of 1 and energy threshold of -5. These settings are noted to give a true positive rate of 43.6%. We cloned CANYA (version2_09-01-2025) from GitHub and installed it on Ubuntu 22.04.5 LTS and predicted the CANYA scores on the local installation. Similarly, we installed TANGO (tango_x86_64_release) on the local machine via an academic license obtained from http://tango.crg.es/ and performed amyloidogenesis prediction. We extracted the top 1% scoring collagen-like domains from PASTA2.0, CANYA, and TANGO outputs and computed the relative abundance of residues in the *X*- and *Y*-positions. The heatmaps depicting the relative abundances were created using an in-house python script that converts the raw counts of observed Gly-*X*-*Y* triplets into percentages of the total. Each matrix cell = (count of that *X*-*Y* pair) ÷ (sum of all pair counts) × 100.

5.2 | Synthesis of Peptides

All peptides were synthesized via solid phase peptide synthesis using cycles of Fmoc-deprotection using piperidine base and amino acid coupling with Oxyma Pure and *N*, *N*-diisopropylcarbodiimide (DIC). Amino acids—glycine (Fmoc-Gly-OH; Iris Biotech 29022-11-5), threonine (Fmoc-L-Thr(OtBu)-OH; Iris Biotech 71989-35-0), alanine (Fmoc-L-Ala-OH; Iris Biotech 35661- 39-3), valine (Fmoc-L-Val-OH; Iris Biotech 68858-20-8), isoleucine (Fmoc-L-Ile-OH; Iris Biotech 71989-23- 6) and leucine (Fmoc-L-Leu-OH; Iris Biotech 35661-60-0)—were dissolved in DMF (*N*,*N*-Dimethylformamide ≥99.8%, AnalaR NORMAPUR; VWR 68-12-2) and coupled to a rink amide resin (Tentagel S RAM Resin; Rapp Polymere GmbH S30023; 0.22–0.24 mmol/g) after activation with 1:0.75 molar ratio mixture of DIC (*N,N'*-Diisopropylcarbodiimide 99%; Sigma–Aldrich 693-13-0) and Oxyma Pure (CEM 3849-21-6). GATGVT-12 and GATGVT-18 were synthesized on a 4-methylbenzhydrylamine (MBHA) resin with a loading of 0.5–1.5 mmol g^{-1} to increase the weight yield of the peptides. Fmoc was deprotected with 10% (v/v) piperidine (≥ 99%, for synthesis; Carl Roth 110-89-4). After coupling of the last amino acid, Fmoc was deprotected, and the resin washed five times with 5 mL of dichloromethane and dried overnight under nitrogen purging. The N-terminal free amine was acetylated with an equimolar mixture of *N*,*N*-diisopropylethylamine and acetic anhydride in dichloromethane for 30 min with two changes of the reactants. The acetylated resin was washed five times with 5 mL dichloromethane and dried overnight by purging nitrogen. Peptide was cleaved off the resin with 10 mL total volume of trifluoroacetic acid (PEPTIPURE ≥99.9%; Carl Roth 76-05-1) containing 0.25 mL triisopropylsilane (98%; Sigma–Aldrich 6485-79-6) and 0.25 mL Milli-Q water. The cleaved peptides were precipitated by dropwise addition to ice-cold diethyl ether (with the exception of GLT discussed below) and filtered using a 0.4 µM polytetrafluoroethylene (PTFE) membrane filter under vacuum. The peptides were washed with 50 mL diethyl ether and dried over vacuum. The dried peptides, which appeared as off-white flakes, were collected and stored without further derivatization for further analysis. Peptide GLT did not precipitate upon lowering the solvent polarity of TFA with diethyl ether. Instead, we precipitated it by dropwise addition into ice-cold water, washed with 50 mL water and recovered the crude peptide without further derivatization.

5.3 | Mass-Spectrometry using Matrix-Assisted Laser Desorption/Ionization Mass Spectrometry (MALDI-MS)

A small granule of each crude peptide was dissolved in Mili-Q water. 1 µL of this solution was mixed with 1 µL of 60

weight percent solution of α-cyano-4-hydroxycinnamic acid in acetonitrile containing 0.1% TFA and spotted onto a ground steel MALDI plate and analyzed on a Bruker micro-TOF spectrometer. Mass spectra were acquired in either linear or reflectron positive ion mode using FlexControl software. The obtained mass spectra were analyzed using mMass v3.2 [62].

5.4 | Peptide Purification

Due to the high content of hydrophobic amino acids, the peptides had limited solubility, which ruled out purification using high-performance liquid chromatography. Instead, we purified the peptides using dialysis to remove impurities like TFA salts and other small organics. All peptides (except GLT discussed below) were ultrasonicated in Milli-Q water at 5 mg/mL concentration for 15–30 min, centrifuged at 10 000 rpm in 2 mL Eppendorf tubes to remove insoluble material, poured into pre-washed dialysis tubes with 100–500 Da molecular weight cut-off (Spectra/Por Dialysis Membrane Biotech CE Tubing; #131048; capacity: 0.32 mL/cm) and dialyzed against 5 liters of Milli-Q water for 3 days with four changes of water. The dialyzed peptide solutions of GAT-42 and GATGVT-42 were flash frozen in liquid nitrogen and lyophilized until a visibly dry peptide was observed. This peptide powder was used for all further analysis. For all other peptides, the dialyzed solutions were used for gelation and characterization.

5.5 | Solubility and Gelation

In case of GAT and GATGVT-42, the lyophilized peptide powder was suspended in Milli-Q water via ultrasonication at ∼ 10 mg/L for 15–30 min and poured into clear dialysis tubes with 100–500 Da molecular weight cut-off and dialyzed against 5 liters of Milli-Q water in a cold room. In the case of the other peptides, crude peptide pellets were dissolved in Mili-Q water, ultrasonicated, and loaded into the dialysis tubes and monitored for 2 days while periodically changing the water. The dialysis against buffers was done in the cold room. In the case of GATGVT gels, reduced temperatures were not needed for inducing gelation, but only to retain the gel integrity over a period of time. Hence, the dialysis was performed in RT. The physical state of the suspension was recorded after 2 days, where no further change was observed. The dialyzed suspension of peptides in the GATGVT series was centrifuged in Thermo Scientific Fresco 17 centrifuge at 13 300 G and 10°C for 10 min to physically crosslink the β-sheet fibers, resulting in hydrogels, while the supernatant was discarded. The prepared hydrogels were stored in the cold room at 4°C for further characterization.

5.6 | Circular Dichroism Spectroscopy

The peptide secondary structures were determined using JASCO-815 CD spectropolarimeter. The concentrations differed based on the amino acid sequence and the length of the peptides. Solutions of GAT, GIT, GLT, and peptides in the GVT series were prepared in Milli-Q water at a concentration of 0.1 mg/mL, while the peptides in the GATGVT series were prepared at 10 mg/mL. Ellipticity was recorded as a function of wavelength (between 250 and 190 nm), as the characteristic triple helix maxima is observed at 225 nm. To obtain the spectra, two types of quartz cuvettes (0.1 cm and 0.001 cm pathlength) were used, depending on the concentration of the sample –0.1 mg/mL and 10 mg/mL, respectively, that was pre-calibrated to 5°C (the experimental temperature). Peltier temperature controller (PTC-423S), attached to the CD spectropolarimeter, was used to monitor and control the temperature of the cuvette holder. The spectrographs were recorded at a bandwidth of 1 nm and scanning rate of 50 nm/min, with a response time of 8 s, data pitch of 0.1 nm, and averaging 3 scans for every data point. The peptides lack chromophores to determine accurate concentrations, while the fibers induce scattering. Thus, the calculation of molar residual ellipticity could not be performed. In order to allow visual comparison of the spectral shape, all curves were normalized such that the peak with maximum intensity is set to unity using GraphPad Prism version 10.

5.7 | Fourier Transform Infrared Spectroscopy (FTIR)

Fourier transform infrared spectroscopy is a common and widely used analytical technique to identify secondary structures of peptide and protein molecules by analyzing their infrared absorption spectra. The measurements were carried out on a Bruker TENSOR 27 FTIR spectrometer with an attenuated total reflectance stage (Pike Technologies; #18717) with a germanium crystal. The instrument was under constant airflow and cooled using liquid nitrogen. The device was operated using OPUS 8.1 software set to Miracle_GE.XPM experiment mode. The sample analysis range was in the mid-infrared region between 4000 and 800 cm^{-1}, and the main region of interest was the amide I band (1700–1600 cm^{-1}) for understanding the secondary structures present in hydrogels. The background compensation was measured with atmospheric air for the instrument to perform baseline and atmospheric components correction. In a typical measurement, a small drop (approximately 10 μL) of the gel sample was placed on the crystal surface and allowed to dry for 5 min to enhance peptide contact with the crystal. The absorbance was recorded in attenuated total reflectance mode. The infrared spectrum was acquired at a resolution of 4 by averaging 100 scans. The obtained spectra were normalized and deconvoluted on OriginPro. The amide I peak (1700–1600 cm^{-1}) was baseline-corrected using a spline operation, and the second derivative graphs were obtained for comparison of the secondary structures [43]. The plots were created using GraphPad Prism version 10.

5.8 | Rheology

The hydrogel samples were tested for rheological properties using the Discovery Hybrid Rheometer (DHR Series; TA Instruments Waters LLC). The rheological properties were measured using a 25 mm stainless-steel parallel plate with a geometry gap of 200 μm. Amplitude and frequency sweeps (oscillation) were recorded at 20°C. For the amplitude sweep, the frequency was fixed at 1.0 Hz with varying strain between 0.1 and 1000%, recording 5 points per decade. Time sweeps were conducted before and after the amplitude and frequency sweeps for 60 and 180 s, respectively, at 0.25% strain and 1.0 Hz frequency.

The hydrogels were loaded on the Peltier stage to measure the rheological properties [63].

5.9 | Atomic Force Microscopy (AFM)

AFM was used to view the microstructures of the GATGVT series peptides. The samples were diluted with Milli-Q water to prevent overcrowding of the microstructures on the surface and to obtain a clear and well-defined image. Approximately 1 µL of the 10 mg/mL sample was resuspended in 40 µL of Milli-Q water. The diluted sample was drop-cast on a mica disc freshly cut out of Muscovite Mica, V-5 (Science Services; #71850-01; 0.15–0.21 mm thick). The sample was allowed to adhere to the mica for 3 to 5 min and blotted from the sides using soft tissue. The mica disc was mounted on a metal disc with carbon tape. The samples were dried overnight before imaging on the Nanosurf Flex Axiom NIR. The images were acquired using the tapping mode with the Tap 190AI—G (Budget Sensors) cantilever under ambient atmosphere. To prevent interference from external vibrations, the device was connected to Isostage 300. The images were acquired at 0.5 s/line raster speed. The height profiles of the peptides obtained were processed using Gwyddion software.

5.10 | Scanning Electron Microscopy (SEM)

The GATGVT peptide assemblies were imaged using SEM to study fiber morphology, packing, and hydrogel porosity. The peptides were cast as discs of ∼2 mm thickness and roughly 0.5 cm diameter on a 2 mL Eppendorf lid and allowed to rest for an hour. The samples were then frozen in liquid nitrogen for 20–30 min. The frozen discs were cracked using a needle and lyophilized overnight (∼24 h). The lyophilized peptides were mounted on SEM stubs with conductive carbon tape. To increase the electric discharge and minimize the charging effect, adhesive aluminum tape was used to connect the sample to the metal stubs. The samples were sputter-coated with platinum for a thickness of 2 nm in an argon vacuum atmosphere using Leica Microsystems EM ACE600 sputter coater. The samples were imaged with FEI/ThermoFisher ApreoVS SEM device at 3 kV employing various detectors. The images were obtained at different magnifications between 25,000 X and 250,000 X. For imaging up to 100 000 X ETD detector was employed, and above 100 000 X T1 and T2 detectors were used.

5.11 | Cell Culture

The cells were thawed and resuspended in freshly prepared 9 mL complete growth media. The cells were 2D cultured and monitored closely with periodic media changes when a change in pH (color change from pinkish red to an orange hue) was observed in the media. The cells were harvested using trypsin and subcultured on reaching approximately 80% confluence to prevent overgrowth. During media change and subculturing, the cells were rinsed with DPBS. After attaining 80%–90% confluence, the cells were harvested using trypsin to detach them from the flask and counted on a Neubauer Chamber post-staining with Trypan blue. The volume of media was calculated to have 1 million cells. It was centrifuged at 200 rpm, and the supernatant was discarded. 500 µl of fresh media was added to the cell pellet, and cells were resuspended. This cell suspension was used to seed the hydrogel. The hydrogel of GATGVT-30 was cast as thin discs of ∼1–1.5 mm thick on an 8-well slide and left to set for an hour at 5°C. The hydrogels were sterilized in the laminar airflow chamber by exposure to UV radiation for 45 min. On the sterilized hydrogels, 50 µL cell suspension was loaded, and the cells were allowed to adhere to the gels for 30 min in the incubator at 37°C. Thereafter, 250 µL of fresh growth media was added to each well. The cell culture was maintained for 1 week to witness cell viability. Media was changed every 24 h in all the wells. Cell viability was calculated using the live/dead assay.

5.12 | Live Dead Assay

For live/dead assay, the cells were stained with calcein AM (green; live cells) and ethidium homodimer (red; dead cells) at 0.1% w/v in DPBS. The assay was performed every alternate day, starting from day 1 by staining 2 wells for each imaging. The cells were washed with DPBS twice, and then 200 µL of staining solution was added to the 2 wells for imaging, while fresh media was added to the other wells. The culture slide was incubated for 30 min. After incubation, the stain was removed, and the cells were washed with DPBS, and fresh media was added to the stained hydrogels. The cells were imaged under a fluorescent microscope (Leica DMi8 microscope; LAS-X software) using FTC and TXR filters to view live and dead cells, respectively. The procedure was carried out in the dark as the stains were light-sensitive. The images were used to calculate the number of live and dead cells using ImageJ software. The cell viability is reported in terms of percentage.

Acknowledgements

This research was funded by the Deutsche Forschungsgemeinschaft [DFG, German Research Foundation, grant number: 326998133-TRR 225 (C01) to Thomas Scheibel]. The authors further acknowledge the financial support of the Technologie Allianz Oberfranken (TAO). We also thank Alexandra Pellert for guidance in setting up the cell culture experiments, Johannes Diehl and Nicole Diehl for assistance in peptide synthesis and Dr Martin Humenik for training AAJ and VS on the AFM. [Correction added on April 15, 2026, after first online publication: Acknowledgement Section has been corrected.]

Open access funding enabled and organized by Projekt DEAL.

Conflicts of Interest

The authors declare no conflict of interest.

Data Availability Statement

The data that support the findings of this study are available from the corresponding author upon reasonable request.

References

1. M. F. Moradali and B. H. A. Rehm, "Bacterial Biopolymers: From Pathogenesis to Advanced Materials," *Nature Reviews Microbiology* 18 (2020): 195–210.

2. Y. Shen, A. Levin, A. Kamada, et al., "From Protein Building Blocks to Functional Materials," *ACS Nano* 15 (2021): 5819–5837.

3. L. A. Estrella, E. A. Yates, K. P. Fears, et al., "Engineered Escherichia coli Biofilms Produce Adhesive Nanomaterials Shaped by a Patterned 43 kDa Barnacle Cement Protein," *Biomacromolecules* 22 (2021): 365–373.

4. F. Li, L. Ye, L. Zhang, et al., "Design of a Genetically Programmed Barnacle-Curli Inspired Living-Cell Bioadhesive," *Materials Today Bio* 14 (2022): 100256.

5. P. Q. Nguyen, Z. Botyanszki, P. K. R. Tay, and N. S. Joshi, "Programmable Biofilm-based Materials from Engineered Curli Nanofibres," *Nature Communications* 5 (2014): 1–10.

6. D. Li, Y. Zhu, T. Yang, M. Yang, and C. Mao, "Genetically Engineered Flagella Form Collagen-like Ordered Structures for Inducing Stem Cell Differentiation," *Iscience* 17 (2019): 277–287.

7. A. W. Nowakowska, J. W. Wojciechowski, N. Szulc, and M. Kotulska, "The Role of Tandem Repeats in Bacterial Functional Amyloids," *Journal of Structural Biology* 215 (2023): 108002.

8. X. Wang and M. R. Chapman, "Sequence Determinants of Bacterial Amyloid Formation," *Journal of Molecular Biology* 380 (2008): 570–580.

9. J. Cámara-Almirón, L. Domínguez-García, N. El Mammeri, et al., "Molecular Characterization of the N-terminal Half of TasA During Amyloid-Like Assembly and Its Contribution to Bacillus Subtilis Biofilm Formation," *Biofilms Microbiomes* (2023): 9.

10. A. Taglialegna, S. Navarro, S. Ventura, et al., "Staphylococcal Bap Proteins Build Amyloid Scaffold Biofilm Matrices in Response to Environmental Signals," *PLoS Pathogens* 12 (2016): 1–34.

11. A. Taglialegna, L. Matilla-Cuenca, P. Dorado-Morales, et al., "The Biofilm-associated Surface Protein Esp of Enterococcus faecalis Forms Amyloid-Like Fibers," *npj Biofilms and Microbiomes* 6 (2020): 1–12.

12. S. Perov, O. Lidor, N. Salinas, et al., "Structural Insights Into curli CsgA Cross-β Fibril Architecture Inspire Repurposing of Anti-amyloid Compounds as Anti-biofilm Agents," *PLOS Pathogens* 15 (2019): 1007978.

13. P. Lembré, C. Vendrely, and P. Martino, "Identification of an Amyloidogenic Peptide from the Bap Protein of Staphylococcus epidermidis," *Protein & Peptide Letters* 21 (2013): 75–79.

14. R. Nelson, M. R. Sawaya, M. Balbirnie, et al., "Structure of the Cross-β Spine of Amyloid-Like Fibrils," *Nature* 435 (2005): 773–778.

15. T. A. Linden and N. King, "Widespread Distribution Of Collagens and Collagen-Associated Domains In Eukaryotes," *bioRxiv* (2021), https://doi.org/10.1101/2021.10.08.463732.

16. A. V. Persikov, J. A. M. Ramshaw, A. Kirkpatrick, and B. Brodsky, "Amino Acid Propensities for the Collagen Triple-helix," *Biochemistry* 39 (2000): 14960–14967.

17. Y. Qiu, C. Zhai, L. Chen, X. Liu, and J. Yeo, "Current Insights on the Diverse Structures and Functions in Bacterial Collagen-Like Proteins," *ACS Biomaterials Science & Engineering* 9 (2023): 3778–3795.

18. M. Rasmussen, M. Jacobsson, and L. Björck, "Genome-based Identification and Analysis of Collagen-related Structural Motifs in Bacterial and Viral Proteins," *Journal of Biological Chemistry* 278 (2003): 32313–32316.

19. J. D. Malcor, N. Ferruz, S. Romero-Romero, S. Dhingra, V. Sagar, and A. A. Jalan, "Deciphering the Folding Code of Collagens," *Nature Communications* 16 (2025): 2702.

20. S. J. Todd, A. J. G. Moir, M. J. Johnson, and A. Moir, "Genes of Bacillus Cereus and Bacillus Anthracis Encoding Proteins of the Exosporium," *Journal of Bacteriology* 185 (2003): 3373–3378.

21. E. Maes, F. Krzewinski, E. Garenaux, et al., "Glycosylation of BclA Glycoprotein From Bacillus Cereus and Bacillus Anthracis Exosporium Is Domain-specific," *Journal of Biological Chemistry* 291 (2016): 9666–9677.

22. N. Zhao, Y. Ge, T. Shi, X. Hu, and Z. Yuan, "Collagen-Like Glycoprotein bclS Is Involved in the Formation of Filamentous Structures of the Lysinibacillus Sphaericus Exosporium," *Applied and Environmental Microbiology* 80 (2014): 6656–6663.

23. L. N. Waller, M. J. Stump, K. F. Fox, et al., "Identification of a Second Collagen-Like Glycoprotein Produced by Bacillus Anthracis and Demonstration of Associated Spore-specific Sugars," *Journal of Bacteriology* 187 (2005): 4592–4597.

24. J. M. Daubenspeck, H. Zeng, P. Chen, et al., "Novel Oligosaccharide Side Chains of the Collagen-Like Region of BclA, the Major Glycoprotein of the Bacillus Anthracis Exosporium," *Journal of Biological Chemistry* 279 (2004): 30945–30953.

25. J. G. Bann, D. H. Peyton, and H. P. Bächinger, "Sweet is Stable: Glycosylation Stabilizes Collagen," *FEBS Letters* 473 (2000): 237–240.

26. X. Zhao, Y. Wang, Q. Shang, et al., "Collagen-Like Proteins (ClpA, ClpB, ClpC, and ClpD) Are Required for Biofilm Formation and Adhesion to Plant Roots by Bacillus amyloliquefaciens FZB42," *PLoS ONE* 10 (2015): 1–16.

27. M. Varadi, G. De Baets, W. F. Vranken, P. Tompa, and R. Pancsa, "AmyPro: A Database of Proteins With Validated Amyloidogenic Regions," *Nucleic Acids Research* 46 (2018): D387–D392.

28. R. Dec and W. Dzwolak, "A Tale of Two Tails: Self-Assembling Properties of A- and B-chain Parts of Insulin's Highly Amyloidogenic H-fragment," *International Journal of Biological Macromolecules* 186 (2021): 510–518.

29. E. P. Barykin, I. Y. Petrushanko, S. A. Kozin, et al., "Phosphorylation of the Amyloid-Beta Peptide Inhibits Zinc-Dependent Aggregation, Prevents Na,K-ATPase Inhibition, and Reduces Cerebral Plaque Deposition," *Frontiers in Molecular Neuroscience* 11 (2018): 1–11.

30. Y. Li, W. Liu, R. Wang, et al., "Chemical Synthesis Uncovers the Significant Impact of Natural Glycosylation on Islet Amyloid Polypeptide Aggregation," *Science Advances* 11 (2025): 1–10.

31. X. Xiao, A. S. Robang, S. Sarma, et al., "Sequence Patterns and Signatures: Computational and Experimental Discovery of Amyloid-forming Peptides," *PNAS Nexus* 1 (2022): 1–12.

32. S. O. Garbuzynskiy, M. Y. Lobanov, and O. V. Galzitskaya, "FoldAmyloid: A Method of Prediction of Amyloidogenic Regions From Protein Sequence," *Bioinformatics* 26 (2009): 326–332.

33. R. Prabakaran, P. Rawat, S. Kumar, and M. Michael Gromiha, "ANuPP: A Versatile Tool to Predict Aggregation Nucleating Regions in Peptides and Proteins," *Journal of Molecular Biology* 433 (2021): 166707.

34. M. Thompson, M. Martín, T. S. Olmo, et al., "Massive Experimental Quantification Allows Interpretable Deep Learning of Protein Aggregation," *Science Advances* 11 (2025): 1–16.

35. I. Walsh, F. Seno, S. C. E. Tosatto, and A. Trovato, "PASTA 2.0: An Improved Server for Protein Aggregation Prediction," *Nucleic Acids Research* 42 (2014): W301–W307.

36. A. M. Fernandez-Escamilla, F. Rousseau, J. Schymkowitz, and L. Serrano, "Prediction of Sequence-dependent and Mutational Effects on the Aggregation of Peptides and Proteins," *Nature Biotechnology* 22 (2004): 1302–1306.

37. Y. Lequette, E. Garénaux, T. Combrouse, et al., "Domains of BclA, the Major Surface Glycoprotein of the B. cereus Exosporium: Glycosylation Patterns and Role in Spore Surface Properties," *Biofouling* 27 (2011): 751–761.

38. T. C. Kuo, P. C. Lee, C. W. Tsai, and W. Y. Chen, "Salt Bridge Exchange Binding Mechanism between Streptavidin and its DNA Aptamer—Thermodynamics and Spectroscopic Evidences," *Journal of Molecular Recognition* 26 (2013): 149–159.

39. A. Micsonai, F. Wien, L. Kernya, et al., "Accurate Secondary Structure Prediction and Fold Recognition for Circular Dichroism Spectroscopy," *Proceedings of the National Academy of Sciences* 112 (2015): E3095–E3103.

40. Y. Liu, S. Ling, S. Wang, X. Chen, and Z. Shao, "Thixotropic Silk Nanofibril-based Hydrogel with Extracellular Matrix-like Structure," *Biomaterials Science* 2, no. 10 (2024): 1338–1345, https://doi.org/10.1039/C4BM00214H.

41. E. K. Roberts, K. M. Wong, E. J. Lee, M. M. Le, D. M. Patel, and A. K. Paravastu, "Post-assembly α-helix to β-sheet Structural Transformation within SAF-p1/p2a Peptide Nanofibers," *Soft Matter* 14 (2018): 8986–8996.

42. R. I. Litvinov, D. A. Faizullin, Y. F. Zuev, and J. W. Weisel, "The α-helix to β-sheet Transition in Stretched and Compressed Hydrated Fibrin Clots," *Biophysical Journal* 103 (2012): 1020–1027.

43. T. F. Kumosinski and H. M. Farrell, "Determination of the Global Secondary Structure of Proteins by Fourier Transform Infrared (FTIR) Spectroscopy," *Trends in Food Science & Technology* 4 (1993): 169–175.

44. K. Hyun, M. Wilhelm, C. O. Klein, et al., "A Review of Nonlinear Oscillatory Shear Tests: Analysis and Application of Large Amplitude Oscillatory Shear (LAOS)," *Progress in Polymer Science* 36 (2011): 1697–1753.

45. D. Gan, T. Xu, W. Xing, et al., "Mussel-Inspired Contact-Active Antibacterial Hydrogel with High Cell Affinity, Toughness, and Recoverability," *Advanced Functional Materials* 29 (2019): 1–11.

46. S. Jindal, K. Ghosal, B. Khamaisi, N. Kana'an, E. Nassar-Marjiya, and S. Farah, "Facile Green Synthesis of Zingerone Based Tissue-Like Biodegradable Polyester with Shape-Memory Features for Regenerative Medicine," *Advanced Functional Materials* 34 (2024): 1–19.

47. R. Song, X. Wang, M. Johnson, et al., "Enhanced Strength for Double Network Hydrogel Adhesive through Cohesion-Adhesion Balance," *Advanced Functional Materials* 34 (2024): 1–9.

48. K. S. Koeck, V. T. Trossmann, and T. Scheibel, "3D-Printed and Recombinant Spider Silk Particle Reinforced Collagen Composite Scaffolds for Soft Tissue Engineering," *Advanced Functional Materials* 35, no. 15 (2025): 1–14, https://doi.org/10.1002/adfm.202407760.

49. M. S. Dueholm, S. V. Petersen, M. Sønderkær, et al., "Functional amyloid in Pseudomonas," *Molecular Microbiology* 77 (2010): 1009–1020.

50. A. Marcoleta, F. Wien, V. Arluison, R. Lagos, and R. Giraldo, "Bacterial Amyloids," in *eLS* (John Wiley & Sons, Ltd, 2019): 1–9, https://doi.org/10.1002/9780470015902.a0028401.

51. Ü. Akbey and M. Andreasen, "Functional Amyloids from Bacterial Biofilms—Structural Properties and Interaction Partners," *Chemical Science* 13 (2022): 6457–6477.

52. S. Zhang, T. C. Holmes, C. M. DiPersio, R. O. Hynes, X. Su, and A. Rich, "Self-complementary Oligopeptide Matrices Support Mammalian Cell Attachment," *Biomaterials* 16 (1995): 1385–1393.

53. T. C. Holmes, S. De Lacalle, X. Su, G. Liu, A. Rich, and S. Zhang, "Extensive Neurite Outgrowth and Active Synapse Formation on Self-assembling Peptide Scaffolds," *Proceedings of the National Academy of Sciences* 97 (2000): 6728–6733.

54. J. Reguera, A. Fahmi, P. Moriarty, A. Girotti, and J. C. Rodríguez-Cabello, "Nanopore Formation by Self-assembly of the Model Genetically Engineered Elastin-Like Polymer $[(VPGVG)_2(VPGEG)(VPGVG)_2]$ 15," *Journal of the American Chemical Society* 126 (2004): 13212–13213.

55. M. R. Caplan, E. M. Schwartzfarb, S. Zhang, R. D. Kamm, and D. A. Lauffenburger, "Effects of Systematic Variation of Amino Acid Sequence on the Mechanical Properties of a Self-assembling, Oligopeptide Biomaterial," *Journal of Biomaterials Science, Polymer Edition* 13 (2002): 225–236.

56. H. Zhang, D. Xu, Y. Zhang, M. Li, and R. Chai, "Silk Fibroin Hydrogels for Biomedical Applications," *Smart Medicine* 1 (2022): 20220011.

57. A. Lechner, V. T. Trossmann, and T. Scheibel, "Impact of Cell Loading of Recombinant Spider Silk Based Bioinks on Gelation and Printability," *Macromolecular Bioscience* 22 (2022): 1–10.

58. R. Kananavičiūtė, K. Kvederavičiūtė, D. Dabkevičienė, G. Mackevičius, and N. Kuisienė, "Collagen-Like Sequences Encoded by Extremophilic and Extremotolerant Bacteria," *Genomics* 112 (2020): 2271–2281.

59. M. Zairi, A. C. Stiege, N. Nhiri, E. Jacquet, and P. Tavares, "The Collagen-Like Protein gp12 Is a Temperature-dependent Reversible Binder of SPP1 Viral Capsids," *Journal of Biological Chemistry* 289 (2014): 27169–27181.

60. Z. Yu, B. An, J. A. M. Ramshaw, and B. Brodsky, "Bacterial Collagen-Like Proteins That Form Triple-helical Structures," *Journal of Structural Biology* 186 (2014): 451–461.

61. W. Li, L. Jaroszewski, and A. Godzik, "Clustering of Highly Homologous Sequences to Reduce the Size of Large Protein Databases," *Bioinformatics* 17 (2011): 282–283.

62. M. Strohalm, D. Kavan, P. Novák, M. Volný, and V. Havlíček, "Mass 3: A Cross-platform Software Environment for Precise Analysis of Mass Spectrometric Data," *Analytical Chemistry* 82 (2010): 4648–4651.

63. C. Yan and D. J. Pochan, "Rheological Properties of Peptide-based Hydrogels for Biomedical and Other Applications," *Chemical Society Reviews* 39 (2010): 3528–3540.

Supporting Information

Additional supporting information can be found online in the Supporting Information section.

Supporting File: adfm74173-sup-0001-SuppMat.docx.